1

Stereoscopic PIV and Its Applications on Reconstruction Three-Dimensional Flow Field

L. Gan
Department of Engineering, University of Cambridge
United Kingdom

1. Introduction of stereoscopic PIV

Various concepts involving in the stereoscopic PIV are very briefly summarised in this section. For more details, readers are recommended to read Lavision (2007); Prasad (2000); Raffel et al. (2007). Stereoscopic PIV adopts two digital cameras viewing at the same laser illuminated plane[1] from two different angles to resolve the three velocity components on the plane; see figure 1. Sometimes it is also called 2D3C (two-dimension three-component) PIV. The basic principle of stereoscopic PIV is similar to a pair of human eyes simultaneously observing an object to capture its movement in a plane as well as in the third direction. One major difference to the two-dimensional PIV is that the illuminated plane cannot be too thin, because the third component needs to be resolved. It should allow most of the particles to remain in the illuminated volume after the PIV Δt, to give valid cross-correlation signals for calculating the third component.

1.1 Principle

In this arrangement, the two cameras simultaneously accept a pair of laser exposures to do normal two-dimensional PIV independently. Because the common field of view (FOV) of the

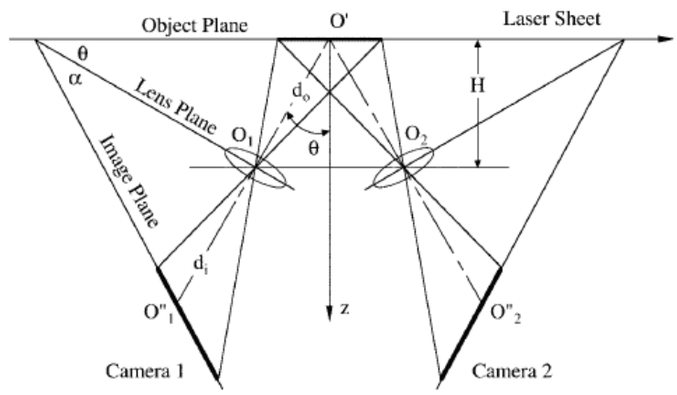

Fig. 1. A schematic diagrame of a typical stereoscopic PIV setup. Picture taken from Prasad (2000).

[1] Strictly speaking, it is not a plane, but a very thin volume with a typical thickness of $2-5mm$.

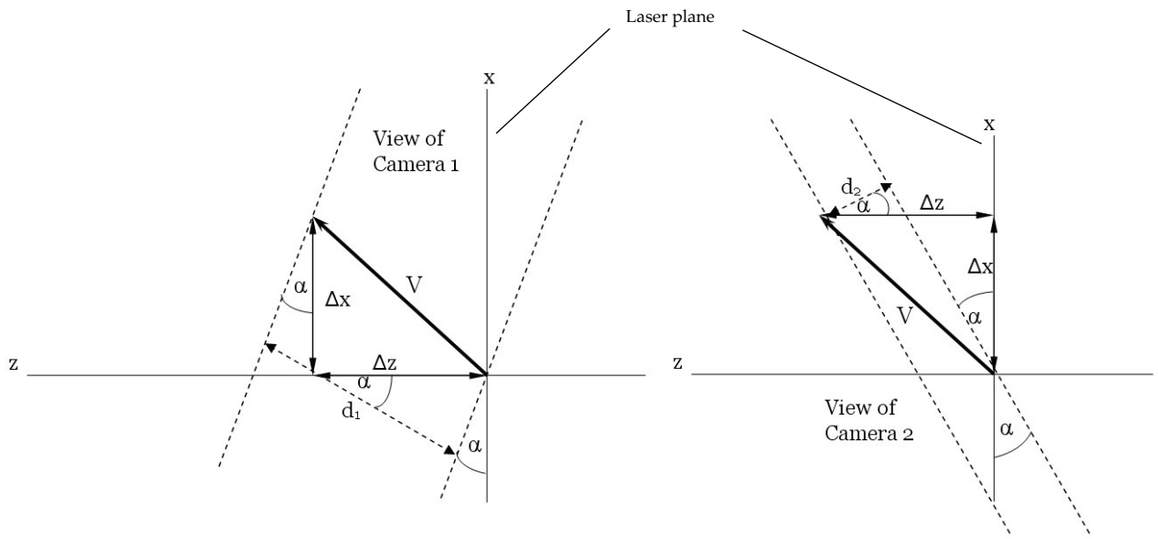

Fig. 2. Reconstructions of displacements seen from the two cameras.

two cameras are maximized[2], the resultant velocity vector fields from the two cameras are combined and from which the 2D3C field is reconstructed, provided a successful stereoscopic calibration having been applied.

The relationships between the real particle displacements (Δx and Δz) and the pixel displacements seen in each of the cameras (d_1 and d_2) can be worked out simply by considering the geometries, as shown in figure 2. For camera 1,

$$d_1 = \Delta z \cos\alpha + \Delta x \sin\alpha; \tag{1}$$

for camera 2,

$$d_2 = \Delta z \cos\alpha - \Delta x \sin\alpha; \tag{2}$$

therefore the true displacements can be re-written in terms of pixel displacements, once the viewing angle is known, as

$$\begin{aligned} \Delta x &= \frac{d_1 - d_2}{2\cos\alpha} \\ \Delta z &= \frac{d_1 + d_2}{2\sin\alpha}. \end{aligned} \tag{3}$$

The displacements in the physical space can be obtained by a simple calibration of d_1 and d_2 to their corresponding displacements in physical space.

However, in most situations, the viewing angles are difficult to measure and moreover, if the experiments are carried out in water, as the viewing angle deviates from 90^o, the image distortion becomes severer. This requires a robuster calibration process.

[2] The two cameras can be located either on the same side (FB [forward-backward scattering] setup, like it shown in figure 1) or on different sides (FF [forward-forward scattering] or BB [backward-backward scattering] setup) of the plate. In the first case, the two FOVs are not possible to be the same; while the second type of setup it is possible to make the FOV almost the same.

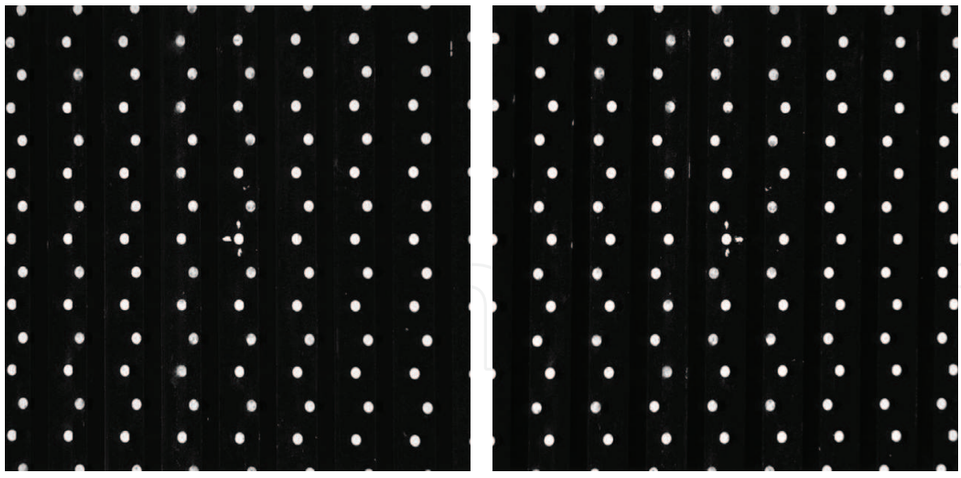

Fig. 3. Calibration plate images viewed from the two cameras. The viewing angle of the two cameras in this case is about 30^o each.

1.2 Calibration

To calibrate the cameras for stereoscopic PIV, one typically needs to take an image of the calibration plate (a plate with a two-dimensional array of circular or cross-shaped markers, which is necessary for correcting distortions), then shift the plate in the plane-normal direction for a small amount and take a second image of it. The amount of shift should be comparable to the laser sheet thickness, as mentioned above, typically around $2-5mm$, depending on and limiting by various situations. Because the amount of shift needs to be very accurate, it is recommended to use a two-level calibration plate as it shown in figure 3, without any need to shift.

To take into account the possible distortion, a third-ordered polynomial fitting function is applied for mapping the global coordinates of the markers on the plate to the associated pixel locations of them. One can also adopts higher ordered polynomial functions, but usually third-order is sufficient. If a third-ordered polynomial function is used, the mapping function typically looks like equation 4, as used in Lavision (2007).

$$\begin{bmatrix} X \\ Y \end{bmatrix} = \begin{bmatrix} a_o + a_1 s + a_2 s^2 + a_3 s^3 + a_4 t + a_5 t^2 + a_6 t^3 + a_7 st + a_8 s^2 t + a_9 s t^2 \\ b_o + b_1 s + b_2 s^2 + b_3 s^3 + b_4 t + b_5 t^2 + b_6 t^3 + b_7 st + b_8 s^2 t + b_9 s t^2 \end{bmatrix}, \tag{4}$$

where X and Y are physical coordination array of the markers on the calibration plate, with the image size $nx \times ny$, the origin location (x_o, y_o) and the normalized pixel location:

$$\begin{aligned} s &= \frac{2(x - x_o)}{nx} \\ t &= \frac{2(y - y_o)}{ny}. \end{aligned} \tag{5}$$

To solve this matrix for the unknown coefficients, one needs sufficient number of markers; if there are more markers than necessary, a least-squares fit will be applied. This fitting process is carried out for each image in the two different normal (z) locations for both cameras (two sets of coefficients for each camera). After the calibration is done, the angles of the line-of-sight

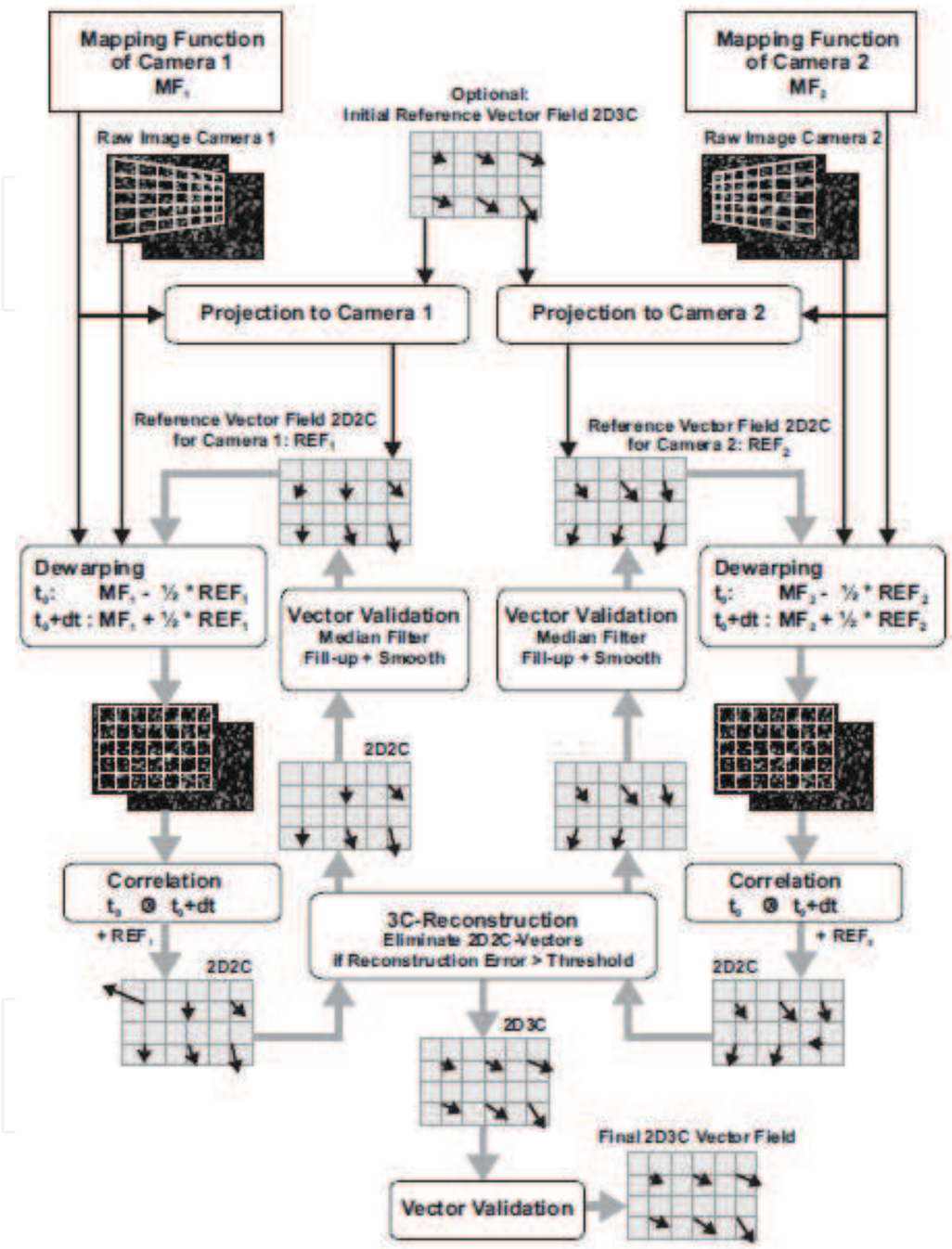

Fig. 4. The flowchart of the computation of 2D3C vector fields adopted in Lavision (2007).

(α in equation 3) of each camera should be known, or one can use this mapping function to reconstruct the 2D3C velocity field directly based on the two-dimensional PIV vectors calculated in each camera, e.g. figure 4 illustrates how Lavision (2007) does this computation.

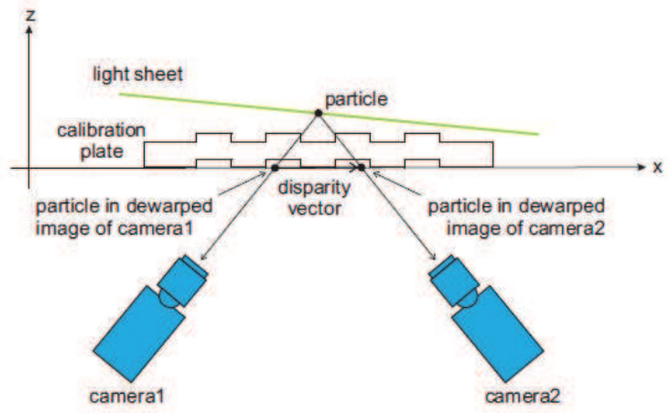

Fig. 5. The concept of disparity vectors, due to the mis-alignment of the laser sheet and the calibration plate surface. Figure taken from Lavision (2007).

1.3 Self-calibration

Stereoscopic self-calibration is useful when there is an imperfection in the calibration process discussed in section 1.2: the laser sheet may not align perfectly with the calibration plate surface. In this case, disparity vectors will appear when the images of camera 1 and camera 2 are dewarped[3] and combined by the original calibration; see figure 5. The original calibration coefficients (in the third-ordered polynomial function) will be modified and updated after self-calibration iterations such that the length of the disparity vectors will be minimized (ideally zero disparity vectors everywhere).

The prerequisite for self-calibration is that the calibration process should be done fairly well and one has about 20 or more good quality[4] particle field images from the stereoscopic recordings for the purpose of statistical convergence. A single particle image is typically divided into a grid of 7×7 (or more) sub-windows. In each of these windows, a two-dimensional disparity vector is calculated by seeking the highest disparity signal in the cluster (with respect to the centre of the window). A typical disparity map of an image is shown in figure 6. Based on the disparity map generated by such figures, the calibration coefficients are updated. Then this updated calibration coefficients are used to compute an updated disparity map, and after which calibration will be updated again. Usually a good self-calibration process requires two to three such iterations. To search the possible matching particles, a method similar to particle tracking technique is used (Wieneke, 2005; 2008).

1.4 Focusing problem

Because the two cameras view the FOV at an angle, usually Scheimpflug adapters are needed. When the object, lens and image planes intersect, the FOV in the object plane will be in focus. Depending on the limits of different types of the Scheimpflug adapters, compensation between the camera aperture size and the laser light intensity needs to be considered. The

[3] The concept of dewarping is not introduced in this chapter, readers are referred to Lavision (2007); Prasad (2000); Raffel et al. (2007).

[4] Good quality particle images should be well focused, with proper particle size and density and low background noise level, etc. Image preprocessing is also recommended before applying self-calibration.

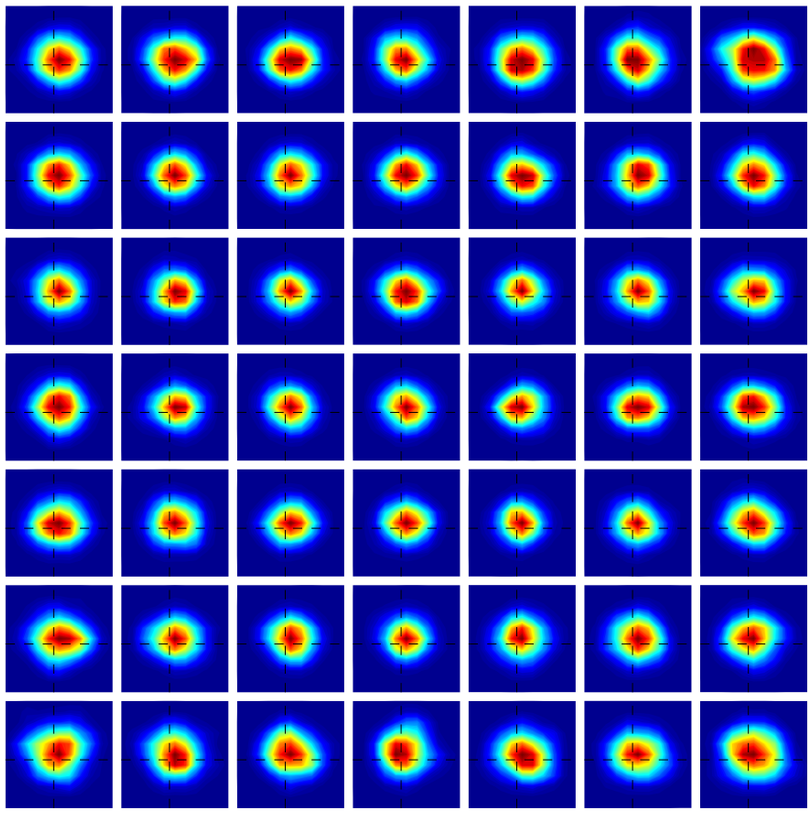

Fig. 6. A typical disparity map. The image window is divided into 7×7 sub-windows. From the peak intensity of each sub-window, a two-dimensional disparity vector can be defined, with respect to the centre of the sub-window. Each sub-window shown in this figure is typically 11×11 $pixel^2$.

viewing angle between a single camera and the laser sheet normal direction usually should not be larger than 60^o, above which the distortion can be too strong and the focusing is difficult even a Scheimpflug adapter is used. In some circumstances, prisms (Prasad, 2000) can also be adopted to help reduce the distortion.

2. An application of stereoscopic PIV: three-dimensional velocity field reconstruction

This section presents an application of stereoscopic PIV to reconstruct a three-dimensional turbulent vortex ring. It is a critical assessment of such an application because a turbulent vortex ring is fully three-dimensional with no preferential direction in the azimuthal plane. Moreover, there is an important property- the translational velocity of a ring is unambiguous.

A vortex ring in laboratory studies is usually generated by an impulsive ejection of fluid through a nozzle or an orifice into a quiescent environment. Circulation based Reynolds number is defined as:

$$Re = \frac{\Gamma_{slug}}{\nu} = \frac{U_p L}{2\nu}. \tag{6}$$

where U_p is the piston velocity and L is the length of the discharged slug, Γ_{slug} is the slug circulation and ν is the kinematic viscosity of the fluid.

Vortex rings which are well-formed at the nozzle or orifice exit, under certain conditions, undergo an instability along the core circumference in the form of azimuthal waves. This type of instability is an important feature of the transition from laminar to turbulent rings. Although previous investigations of this type of waviness have been made in laminar rings or rings during the transition stage from laminar to turbulent Maxworthy (1977); Saffman (1978); Shariff et al. (1994); Widnall & Tsai (1977), the results show that azimuthal waves are also observed in fully turbulent vortex rings and this technique can successfully capture this feature.

2.1 Theoretical background

2.1.1 Taylor's hypothesis

Taylor's hypothesis (Taylor, 1938; Townsend, 1976) states that "if the velocity of the airstream which carries the eddies is very much greater than the turbulent velocity, one may assume that the sequence of changes in U at the fixed point are simply due to the passage of an unchanging pattern of turbulent motion over the point". In other words, if the relative turbulence intensity u' is assumed to be small enough compared to the mean advection speed U:

$$\frac{u'}{U} \ll 1, \tag{7}$$

the time-history of the flow signal from a stationary probe can be regarded as that due to advection of a frozen spatial pattern of turbulence past the probe with the mean advection speed U, i.e.

$$u\left(x,t\right) = u\left(x - U\Delta t, t + \Delta t\right), \tag{8}$$

where Δt is the time delay and should not be a too large value. Taylor's hypothesis is effectively a method to transfer the time dependent measurement results to a spatial domain. The selection of the correct velocity scales relevant to turbulent vortex rings are discussed in section 2.3.

2.1.2 Similarity model

All the figures presented in this chapter are plotted in the similarity coordinates derived from the similarity model (Glezer & Coles, 1990). The reason is because the original model was derived from Taylor's hypothesis. Any structure plotted in the similarity coordinates contains not only spatial but also temporal information: it can be transferred back to the physical coordinates at any point in a series of time history. It has been proved in Gan & Nickels (2010) that rings produced in this study are well predicted by this model.

If a proper pair of spatial and temporal origins z_o, t_o can be found, the length and velocity scales in a turbulent vortex ring in physical space can be shown to be self-similar, and they can be written in terms of the similarity variables, i.e.

$$\xi = \left(z - z_o\right)\left[\frac{\rho}{I\left(t - t_o\right)}\right]^{\frac{1}{4}} \qquad \eta = r\left[\frac{\rho}{I\left(t - t_o\right)}\right]^{\frac{1}{4}}; \tag{9}$$

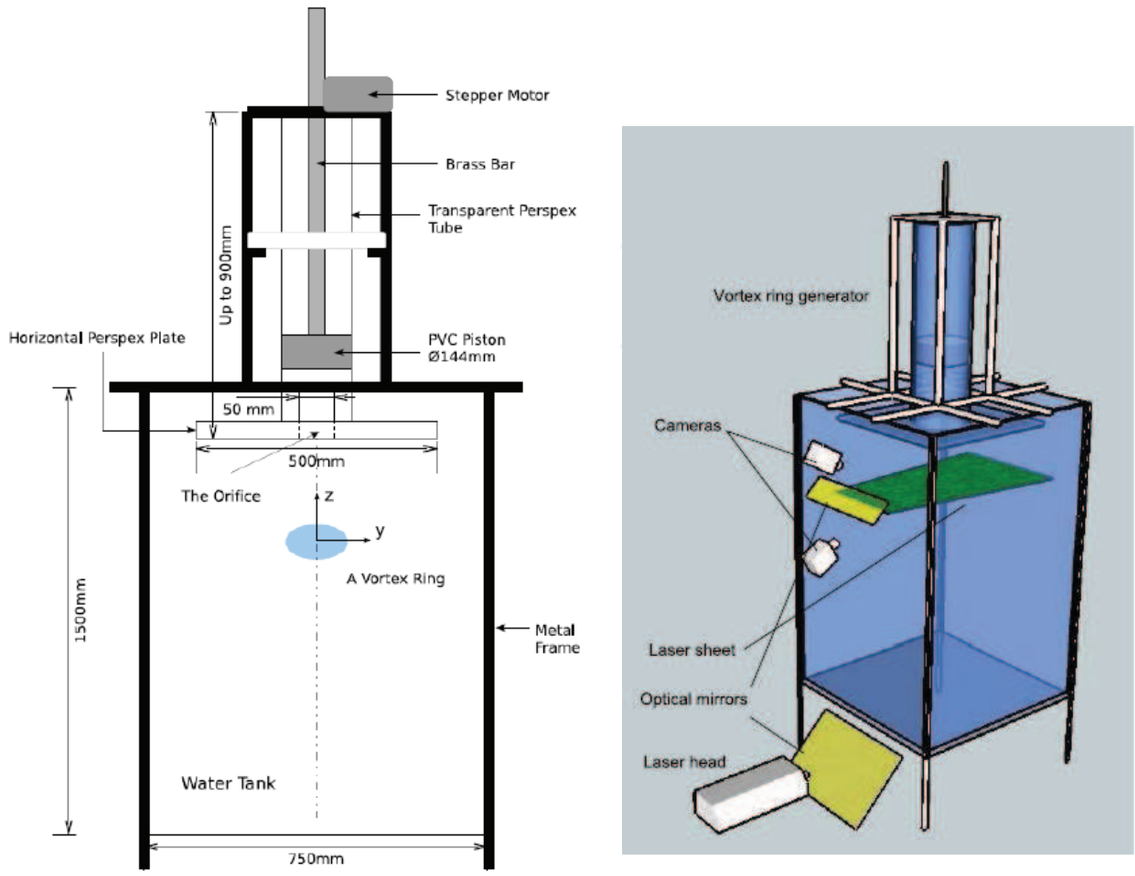

Fig. 7. Schematic diagram of the vortex ring generator. The diagram is not to scale. The coordinate system adopted in this experiment is also shown, where $z = 0$ is set at the orifice exit.

and from the streamfunction,

$$U = u\left(\frac{\rho}{I}\right)^{\frac{1}{4}}(t - t_o)^{\frac{3}{4}} \qquad V = v\left(\frac{\rho}{I}\right)^{\frac{1}{4}}(t - t_o)^{\frac{3}{4}}, \tag{10}$$

where I is the hydrodynamic impulse (assumed invariant); ρ is the density (a constant when incompressibility is assumed); u, v are the radial and axial velocity components respectively; U, V are the corresponding non-dimensional velocities. ξ and η are the non-dimensional similarity quantities for the length scales.

2.2 Experimental setup

A simple sketch of the ring generator is presented in figure 7.

The rectangular tank is made of $15mm$ thick perspex with a bottom cross-sectional area of $750mm \times 750mm$ and a height of $1500mm$. The top of the tank is uncovered. The tank is therefore transparent from all directions of views. Other important geometrical parameters of the vortex generator are labelled in figure 7 and is described in Gan et al. (2011).

The motion of the piston is driven by a stepper motor. The motor is able to drive the piston to move at a constant speed of up to $1000 mms^{-1}$ with an acceleration and deceleration of about $1500 mms^{-2}$.

The effective Re is set to 41280 and $L/D = 3.43$ in order to match the conditions in Glezer & Coles (1990) and Gan & Nickels (2010), because parts of the reconstruction validation will rely on the data in them. The piston velocity programme is approximately a top-hat shape: the piston acceleration/deceleration time is about 10% of the piston total movement duration. Rings produced at this combination of Re and L/D are well in the turbulent region on the transition map (see Glezer, 1988).

In this arrangement, the PIV (laser sheet) plane is located 6D (six orifice diameters) downstream of the orifice exit. The PIV system is provided by LaVision Ltd: a pair of high-speed Photron APX cameras are used as the image recording devices and the particle illumination is realised by a Pegasus PIV Laser which consists of a dual-cavity diode pumped Nd:YLF laser head and is capable of emitting a beam of $527 nm$ wavelength and $10 mJ$ energy. The laser beam is converted to a sheet by passing through a cylindrical diverging lens. The thickness of the sheet can be adjusted by changing the separation of a pair of telescope lenses housed before the cylindrical lens and is set to about $4 - 5 mm$. The flow is seeded by $50 \mu m$ diameter, silver-coated hollow glass spheres.

After the changes in refractive index are considered, the effective angle between the two cameras is approximately 120^o. The two cameras run in single-frame single-exposure mode, and the operation frequency is set at $f = 600 Hz$ giving a $\Delta t = 1.67\ ms$. The interrogation window size for time series cross-correlation process is set to $16 \times 16\ pixel^2$ with a 25% overlap to give a spatial resolution of $\Delta x = \Delta y \approx 1.70 mm$ (based on vector spacing, $\approx 3.4\%$ D) in the PIV plane. The FOV of the PIV plane is about $230 \times 164\ mm^2$.

2.3 Accuracy justification

An important prerequisite for the reconstruction of a turbulent vortex ring using Taylor's hypothesis is to identify appropriate scales of the fluctuating and convective velocities in equation 7.

The relevant convective velocity in this work is the ring advection speed, or celerity, and is obtained from the independent two-dimensional PIV results in Gan & Nickels (2010). The centroid-determined vortex ring radii r and celerities u_t for 50 realisations are reproduced in figure 8. From this figure the spatially averaged celerity (□ data) at various streamwise locations is obtained between $z = 5.5D$ to $z = 6.5D$ and the ensemble averaged ring celerity is obtained by a least-squares fit (blue line) giving: $u_t = 270.34\ mms^{-1} \approx 0.54\ U_p$.

The ring celerity also affects the spatial resolution in the z direction, Δz. The reconstruction of the planar velocity fields in the z direction is selected to give a similar spatial resolution in the $x - y$ plane.

The most straight-forward reconstruction process requires the entire cross-sectional area of the ring bubble to pass normally through the PIV plane with constant celerity. Figure 8 shows that

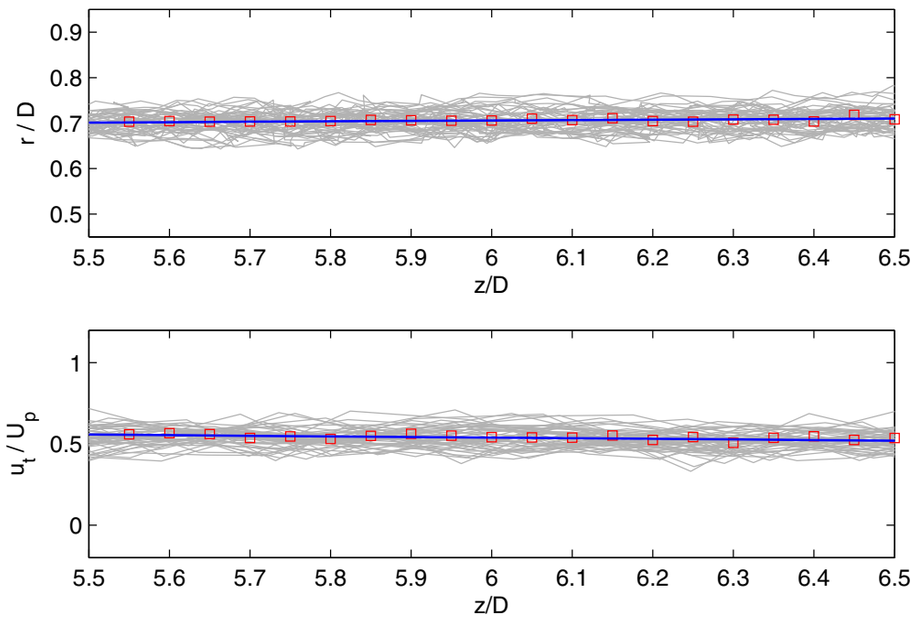

Fig. 8. Ring radius r and celerities u_t as functions of streamwise distances z for the ensemble of 50 realisations from two-dimensional PIV measurements. The grey lines are the traces of each of the 50 realisations; □: the ensemble averaged quantities; −: the first order least squares fit of □. Data are taken from Gan & Nickels (2010).

this condition can be approximated by the ensemble averaged values.[5] The celerities of single realisations are denoted by the grey traces and are always scattered as the ring centroid is changed by the turbulence. This results in a variation of ±10% of the □ value at each location.

If the averaged Reynolds stresses $-\overline{V'V'}$ of the ring bubble is used (from Gan & Nickels, 2010), taking the square root of these and the similarity value of the ring celerity, $U_t = 6.4$ (which can be scaled from u_t in physical space by equation 10), for rings with a $Re = 41280$ (see Table 1 in Gan & Nickels, 2010), equation 7 gives:

$$\frac{u'}{U} = \frac{V'}{U_t} < \frac{0.78}{6.4} \approx 0.12. \tag{11}$$

The maximum error can be estimated using the maximum fluctuation within the ring bubble V' which gives $V'/U_t \approx 0.33$. However, only small contour regions within the ring bubble have this value and these regions will have the largest uncertainty in the reconstruction. A rough estimation of the contribution from u_t fluctuation can also be given by figure 8, which is $u_t'/\overline{u_t} < \pm 10\%$, which according to equation 11 gives a value of 0.2.

A more rigorous method to assess the validity of Taylor's reconstruction is to check whether the material derivative of the velocity vector $D\mathbf{u}/Dt \approx 0$ which is satisfied if $u_t \gg u', v'$ neglecting pressure and viscous terms. The 2D PIV results in Gan & Nickels (2010) are used for

[5] Ideally the instantaneous convection velocity of the ring should be used. This requires simultaneous measurements normal to the measurement plane which were not available.

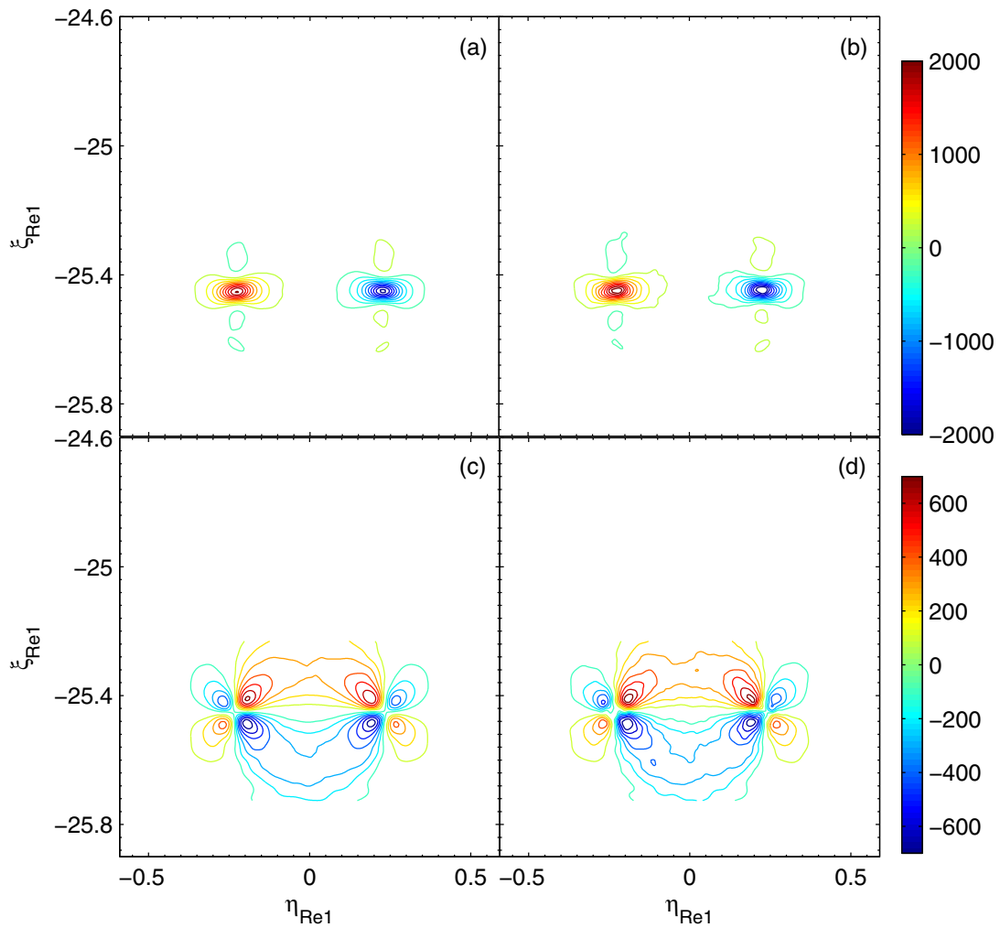

Fig. 9. Test of Taylor's hypothesis by comparing (a): $\left\langle u_t \frac{\partial u}{\partial z} \right\rangle$, (b):$\left\langle -\frac{\partial u}{\partial t} \right\rangle$, (c): $\left\langle u_t \frac{\partial v}{\partial z} \right\rangle$ and (d):$\left\langle -\frac{\partial v}{\partial t} \right\rangle$. Data obtained from two-dimensional PIV measurements. If the Taylor's reconstruction is perfect, contours of these two terms will be identical.

this purpose. The convection terms $\left\langle u_t \frac{\partial u}{\partial z} \right\rangle$ and $\left\langle u_t \frac{\partial v}{\partial z} \right\rangle$ are compared with the acceleration terms $\left\langle -\frac{\partial u}{\partial t} \right\rangle$ and $\left\langle -\frac{\partial v}{\partial t} \right\rangle$ in their non-dimensional forms in figure 9, where

$$\left\langle u_t \frac{\partial \mathbf{u}}{\partial z} \right\rangle = \left(u_t \frac{\partial \mathbf{u}}{\partial z} \right) \left(\frac{\rho}{I} \right)^{\frac{1}{4}} (t - t_o)^{\frac{7}{4}}$$
$$\left\langle -\frac{\partial \mathbf{u}}{\partial t} \right\rangle = \left(-\frac{\partial \mathbf{u}}{\partial t} \right) \left(\frac{\rho}{I} \right)^{\frac{1}{4}} (t - t_o)^{\frac{7}{4}}. \tag{12}$$

Figure 9 shows excellent agreement between the ensemble averaged acceleration and convection terms which lends confidence to the validity of the reconstruction. The good agreement obtained in the similarity coordinates means that Taylor's hypothesis is valid over the rings' time history where the similarity transformation holds.

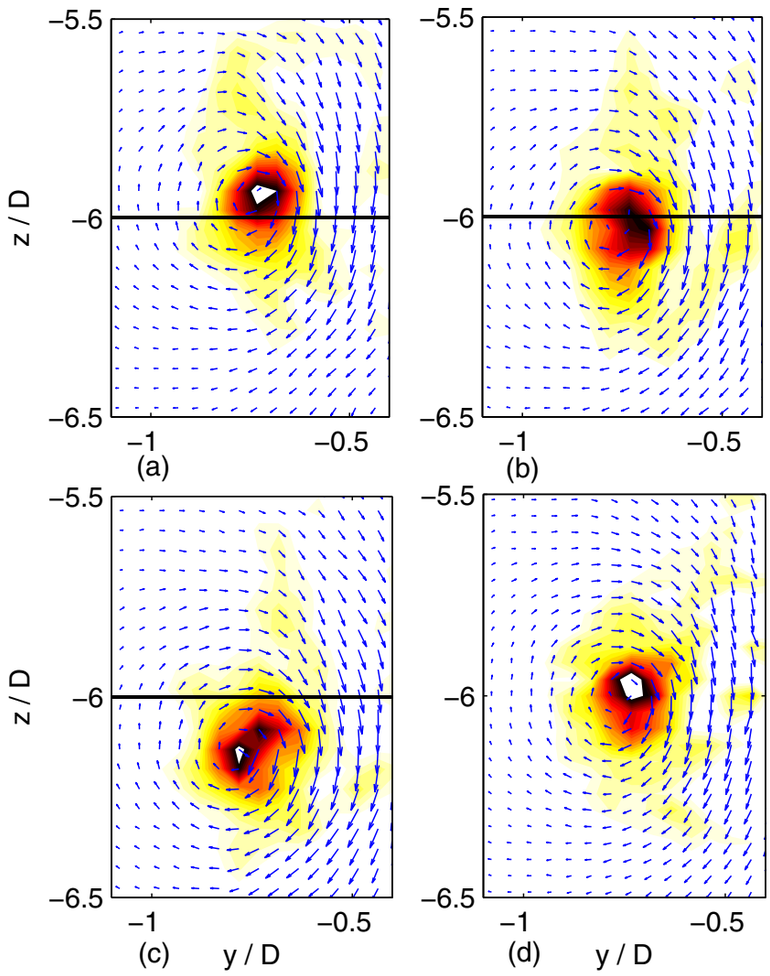

Fig. 10. An individual vortex ring recorded by two-dimensional PIV is used to test the Taylor's reconstruction process. (a), (b), (c): the three continuous snapshots showing the left core of a ring passing through the $6D$ station. The layers of the two-component velocity information at the $6D$ station are then stacked to reconstruct the core, in (d), in which the ensemble averaged ring celerity 270.34 mms^{-1}, instead of the one for this particular ring, is used. The vorticity contour levels: -240.0 (10.0) -20.0; $\rightarrow$ denotes the in-plane velocity vectors.

Figure 10 (a) to (c) plots an image sequence showing a single vortex ring core passing through the 6D station which are then used to reconstruct the vortex core in (d). The velocity vectors are overlaid with vorticity contours. Comparing (a) to (c) with (d) shows that the peak vorticity of the core is basically retained. The vorticity distribution of the inner core shows a slight change in figure 10 (c) but these are small changes and close to the maximum spatial resolution. The instantaneous vorticity is naturally very sensitive to the velocity fluctuation however the core radius remains similar, within $\pm 10\%$, see figure 11. The core is compact being about $0.2D$ in size, passes through the 6D station within about 37 ms. The vorticity surrounding the core is weaker and undergoing shedding-reattachment processes at a fairly fast pace (Gan, 2010). Any high speed fluctuations in the weaker regions are less frozen than the core but their features are well captured in the reconstructed image in figure 10 (d).

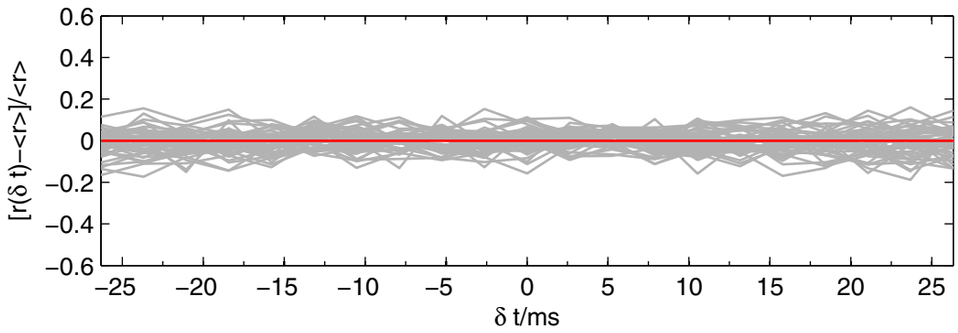

Fig. 11. The core radius variation as the ring passes through the testing station for all the 50 realisations from two-dimensional PIV measurements. The grey lines are the traces of each of the 50 realisations. $r(\delta t)$ denotes the radius of a single realisation as a function of the time t; $\langle r \rangle$ denotes the average radius of all the 50 rings. The threshold to determine the radius is set as $100s^{-1}$, which is about 50% of the peak vorticity intensity, see figure 18. Note that the core passes through the testing station within $\pm 19ms$.

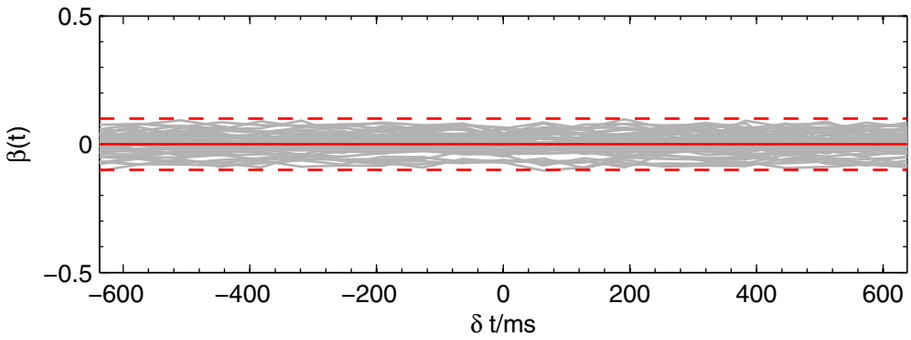

Fig. 12. The circulation variation as the ring passes through the testing station for all the 50 realisations from two-dimensional PIV measurements. The grey lines are the $\beta(t)$ traces for each of the 50 realisations, which is calculated by equation 13. The $\pm 10\%$ lines are also shown by the $--$ traces.

As the largest velocity fluctuations occur around the vortex core, the spatially averaged velocity of 50 realisations can be compared with the reconstructed value. To estimate the spatially averaged velocity error, a quantity $\beta(t)$ is introduced:

$$\beta(t) = \frac{\Gamma(t) - \Gamma_{re}}{\Gamma_{re}} = \frac{\oint_C \mathbf{u}(t) \cdot \mathrm{d}\mathbf{l} - \oint_C \mathbf{u}_{\mathrm{re}} \cdot \mathrm{d}\mathbf{l}}{\oint_C \mathbf{u}_{re} \cdot \mathrm{d}\mathbf{l}}, \tag{13}$$

where Γ is the circulation obtained along a closed loop C enclosing an area of $2D$ and $1.5D$ in streamwise and spanwise directions respectively around each vortex core similar to that shown in figure 10. (t) is the time when the ring passes through the $6D$ station, similar to that shown in (a), (b) and (c) of figure 10. The subscript 're' indicates the reconstructed ring at the $6D$ station as shown in (d) of figure 10. The quantity $\beta(t)$ is determined for 50 realisations and shown in figure 12.

As the loops are of the same size, and the circulation is conserved, $\beta(t)$ compares the spatially-averaged variation between $\mathbf{u}(t)$ of each realisation with the reconstructed one. The resulting error is less than $\pm 10\%$, a similar value to the core dispersion in figure 8 and radius variation in figure 11. The results from these tests show that the expected error of the reconstruction is within $\pm 10\%$.

A more direct assessment is to investigate the divergence field of the reconstructed three-dimensional vortex ring. Figure 13 shows the p.d.f. (probability density function) of the divergence of the flow field, where in (b) and (d) the divergence is normalised by the norm of the local vector gradient tensor $(\nabla \mathbf{u} : \nabla \mathbf{u})^{1/2}$; in (c) κ is defined by:

$$\kappa = \frac{(\partial u/\partial x + \partial v/\partial y + \partial w/\partial z)^2}{(\partial u/\partial x)^2 + (\partial v/\partial y)^2 + (\partial w/\partial z)^2}. \tag{14}$$

It can be seen that most of the data points locate in regions very closed to divergence free, bearing in mind that no experiment is divergence free, due to the finite spatial resolution.

2.4 The reconstructed velocity field

A typical instantaneous stereoscopic PIV velocity - vorticity field is shown in figure 14. Only the in-plane velocity vectors are plotted from which the overlaid vorticity contours ω_k were determined. The level of turbulence is clearly captured by the asymmetry in the vector field and the fluctuations of vorticity.

In order to visualise the vortex ring structure, an appropriate scalar which might be used after Taylor's reconstruction of velocity field is the vorticity ($\nabla \times \vec{u}$) magnitude. The structure of the vortex ring bubble and the wake can then be observed in figure 15 with the strong level of turbulence illustrated by the degree of the wrinkling along the isosurfaces and streamlines. It must be pointed out that in order to visualise the ring bubble by streamlines, the ring needs to be put in a stationary frame of reference. This is achieved by simply subtracting the mean advection velocity of the ring at the PIV testing location[6] from the instantaneous velocity at every data point which has no effect on the vorticity field. In figure 15 the extent of irregularity in the streamline patterns can be distinguished upstream and downstream of the ring bubble with localised areas of high vorticity found in the wake. A wavy core is also observed, confirming the existence of azimuthal waves.

In order to visualise the relationship between the high and low vorticity fluctuations around the vortex ring core and the outer bubble respectively, two sections of the selected bubble vorticity isosurface are shown in figure 16. As expected the low intensity wraps around the core. Tube shaped vorticity isosurfaces of low intensity are shed into the wake showing some agreements with the numerical simulations of Bergdorf et al. (2007) and Archer et al. (2008) which show hairpin vortices being shed from the vortex bubble into the wake. Although, hairpin structures were not clearly observed in the current study. This could be due to the lower spatial resolution of the experiment or the different Reynolds numbers and initial conditions compared with the numerical simulations.

[6] It is assumed here that the ring advection velocity in the vicinity of the PIV testing location is constant. Figure 8 shows that it is a fairly reasonable assumption.

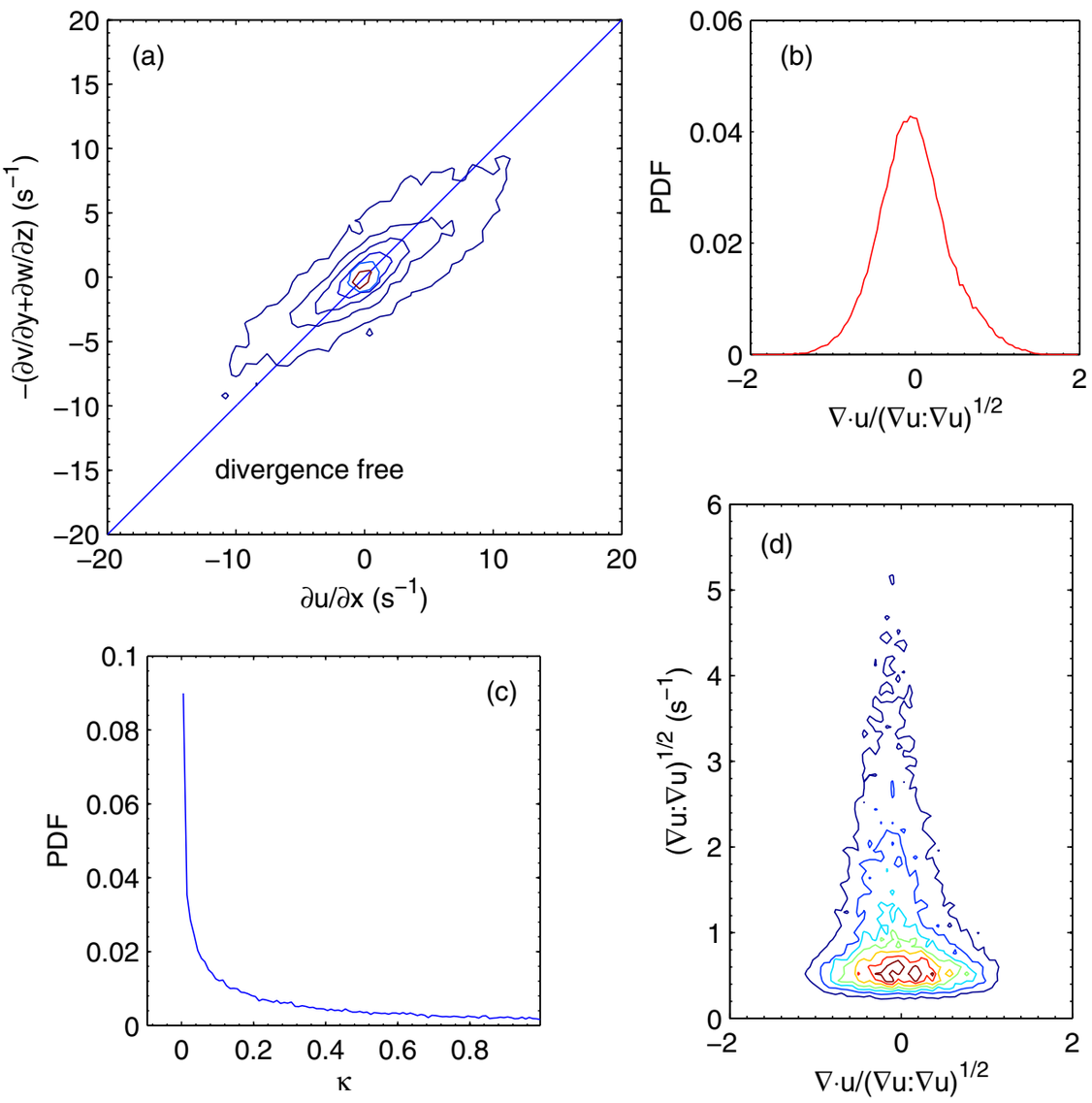

Fig. 13. The divergence of the reconstructed three-dimensional velocity field. (a) the joint p.d.f. between $\partial u/\partial x$ and $-(\partial v/\partial y + \partial w/\partial z)$, contour levels [0.0002 0.0007 0.002 0.007 0.02 0.1]; the straight line indicates divergence free. (b) the p.d.f. of $\nabla \cdot \mathbf{u}/(\nabla \mathbf{u} : \nabla \mathbf{u})^{-1/2}$. (c) the p.d.f. of κ. (d) the joint p.d.f. of $\nabla \cdot \mathbf{u}/\left(\nabla \mathbf{u} : \nabla \mathbf{u}\right)^{1/2}$ and $(\nabla \mathbf{u} : \nabla \mathbf{u})^{1/2}$; contour levels [0.0003 : 0.0003 : 0.003].

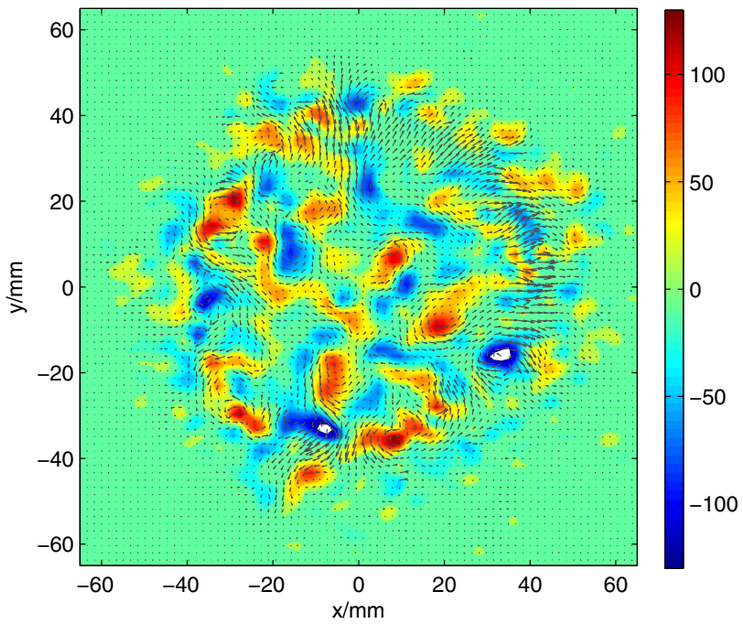

Fig. 14. A presentation of instantaneous velocity and vorticity in azimuthal plane in physical coordinates, when the ring centre is about to reach the PIV plane. Only the velocity vectors in the azimuthal plane are shown. The vorticity is in the streamwise direction, ω_k, zero level bypassed.

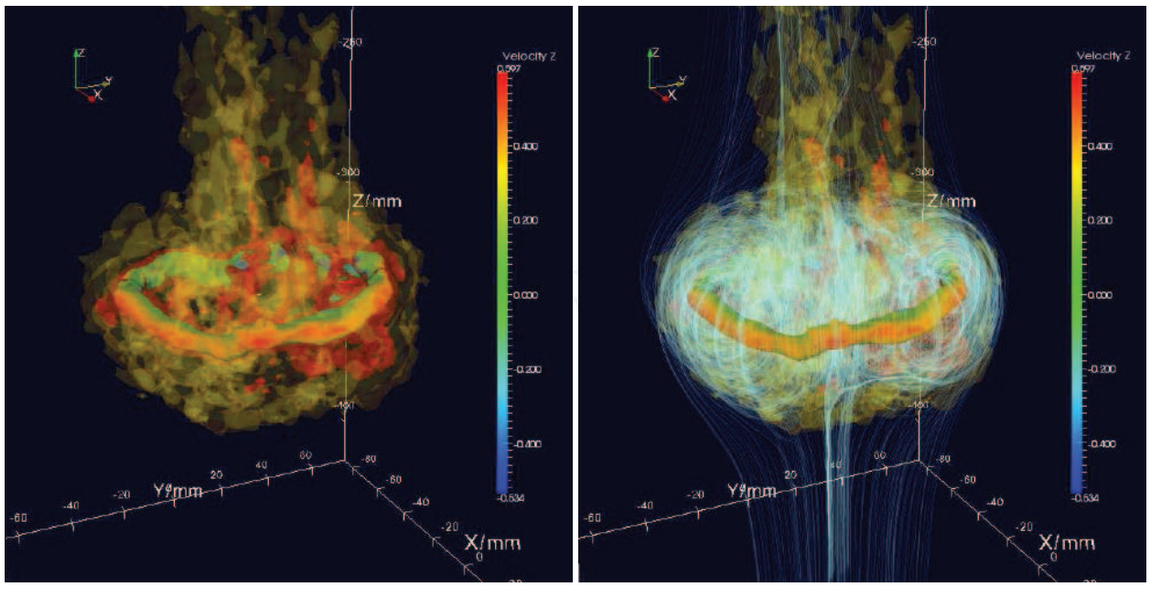

Fig. 15. A three-dimensional vorticity magnitude contour. Isosurface levels are $150s^{-1}$, $100s^{-1}$, $50s^{-1}$. Streamlines are shown in the second figure. The colour bar shows the streamwise velocity level on the core surface.

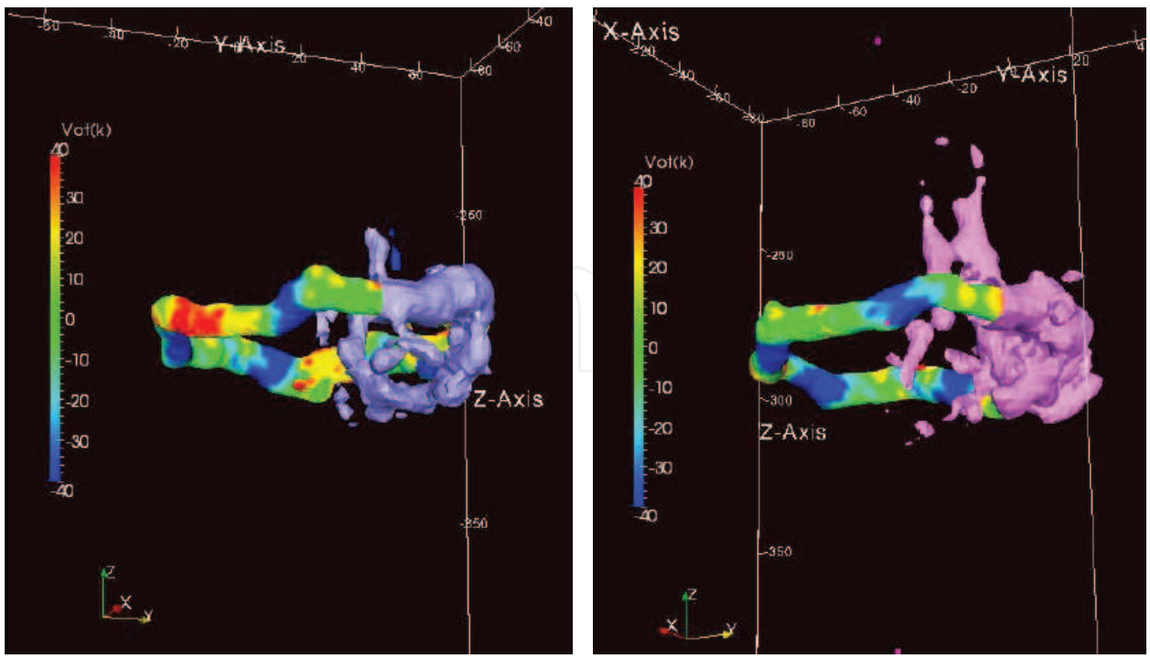

Fig. 16. Isosurfaces of the three-dimensional vorticity magnitude, showing the high intensity core and two portions of the low intensity vorticity blobs wrapping around the core and shed to the wake. Isosurface intensities: $150s^{-1}$ and $90s^{-1}$. Colour code on the core surface indicates the streamwise vorticity ω_k.

The three components of the vorticity, ω_i ω_j ω_k in the two central cross-sectional planes $y-z$ and $x-z$ are plotted in figure 17. The reconstructed azimuthal vorticity contours in (a) and (b) can be compared with the instantaneous vorticity contours obtained from the two-dimensional PIV results, shown in figure 18. Note that Figure 17 and 18 belong to different realisations. Because the rings are very turbulent, contour shapes are noisier especially for low level vorticity, and are expected to be different for different realisations due to the stochastic nature of the flow. However, the main features and the maximum intensities show good agreements with the main difference being that the reconstructed fields show less low level azimuthal vorticity. A long streamwise vorticity ω_k structure is observed in the three-dimensional view in figure 19, which agrees with the findings in Bergdorf et al. (2007). In the ring bubble region, the streamwise vorticity are found to wrap around the vortex core, in a manner such that the positive and the negative valued vortices are separated by each other. This can be seen by the colour code on the core isosurface in figure 16 and shows reasonable agreement with the results in Archer et al. (2008). However, the structure of the vorticity is difficult to identify in the three-dimensional view due to the effect of turbulence which breaks the isosurfaces thresholded at $\omega_k = 30s^{-1}$ into pieces. The colour code on the ω_k isosurface indicates the strength of the streamwise stretching term $S_k = (\vec{\omega} \cdot \nabla)\,\vec{u}_k$. The positive value of ω_k reflects the stretching of the streamwise vortex tubes. The negative valued streamwise vortex tubes are not shown but the structure and the stretching strength of these tubes was found to be similar.

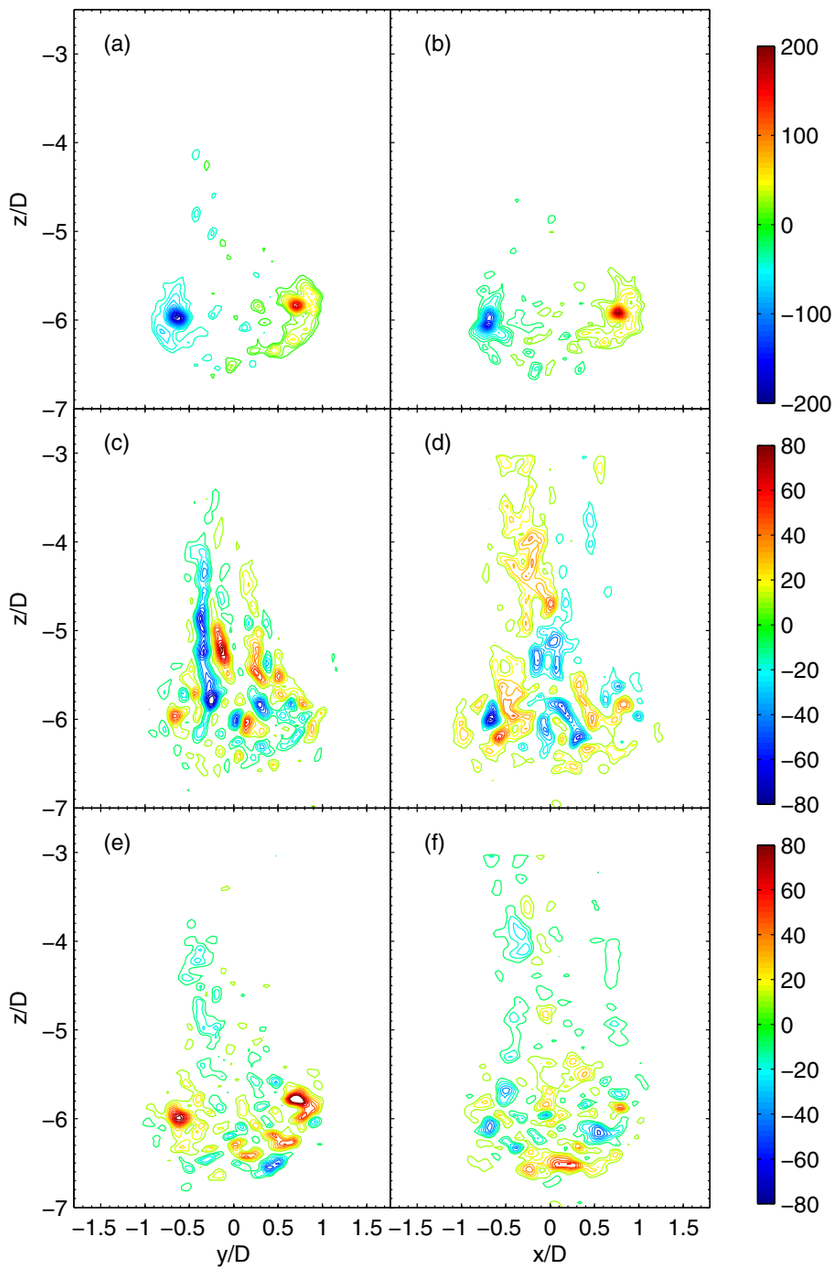

Fig. 17. The three components of vorticity in the two central cross-sectional planes $y - z$ and $x - z$. (a) and (b): azimuthal vorticity contours, ω_i, ω_j; (c) and (d): streamwise vorticity contours, ω_k; (e) and (f): spanwise vorticity contours, ω_j, ω_i.

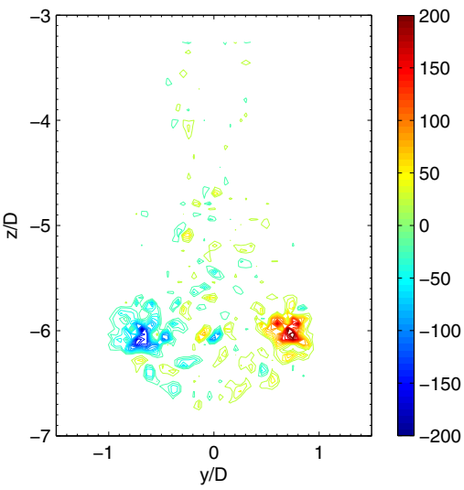

Fig. 18. The vorticity contour of an instantaneous realisation from the two-dimensional PIV experiments.

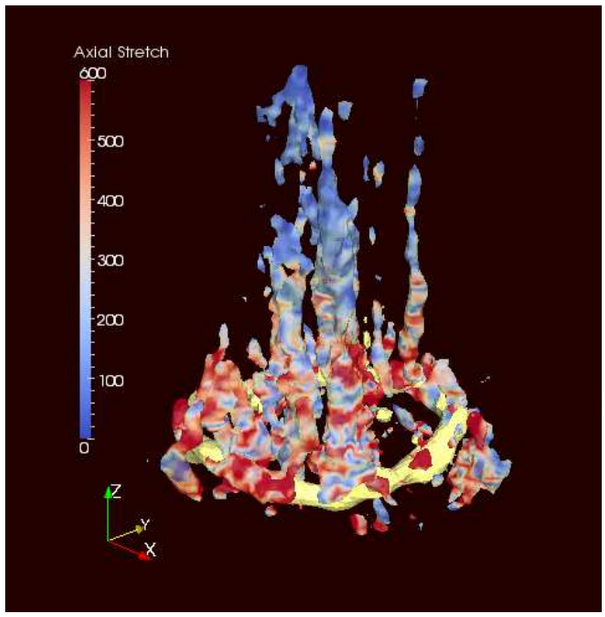

Fig. 19. The streamwise vorticity wraps around the core. The core position is shown by the yellow coloured isosurface of vorticity magnitude $\omega_m = 140s^{-1}$. The vorticity isosurfaces wrapping around the core are $\omega_k = 30s^{-1}$. Colour code on ω_k surface indicates the positive-valued streamwise (axial) vortex stretching term S_k.

2.5 The azimuthally averaged quantities

Statistically speaking, an ensemble-averaged vortex ring bubble tends to be axisymmetric[7]. It is interesting to compare the azimuthally averaged velocity components to those by two-dimensional ensemble averaged ones, which may also serve as a validation of the technique.

The azimuthally averaging process is applied in a cylindrical coordinate system in which the process begins at $\theta = 0$ and ends at $\theta = 2\pi$. The first step is to locate the 'best' centre point, or a proper axis of symmetry as the results from the azimuthally averaging process will depend heavily on the location of this axis. The axis is found by a best r.m.s. fit of the core area to a circle. After this, data format in Cartesian coordinates is converted to cylindrical coordinates. More details can be found in Gan et al. (2011).

The velocities are non-dimensionalised by equation 10 and presented in the similarity coordinates calculated from equation 9. Figure 20 shows the dimensionless velocities U_θ (radial), V_θ (axial), W_θ (azimuthal) and the dimensionless vorticity $\widehat{\omega}_\theta$, where:

$$\widehat{\omega}_\theta = \frac{\partial V_\theta}{\partial \eta} - \frac{\partial U_\theta}{\partial \xi}, \tag{15}$$

and θ here denotes an azimuthally averaging result, ξ, η denote the axial and radial direction in cylindrical coordinates respectively.

In figure 20, noise increases towards the centre due to the reduced number of data points for averaging[8]. However, the main area of interest is obviously the core region. The central region exhibits low azimuthal velocities in figure 20 c): a long region of positive mean velocity is observed in the wake while a weak negative mean velocity can be observed in the core centre region. The presence of a mean velocity in the core region is not surprising, a number of researchers have also observed such behaviour, nevertheless the magnitude is considerably smaller than both the convection velocity V_θ and the radial velocity U_θ components shown in figure 20 a) and b). The opposite sensed mean velocity in the inner region can be partly due to the noise and partly due to a possible mechanism of conservation of angular momentum of the vortex ring bubble. The streamline pattern in figure 15 also suggests the presence of a mean azimuthal velocity.

The dimensionless circulation Γ_θ can be computed by equation 16 from the contour plot in figure 20 d).

$$\Gamma_\theta = \int_S \widehat{\omega}_\theta \, d\xi d\eta, \tag{16}$$

where S denotes the entire area of the FOV in the similarity coordinates. A value of 7.08 is found, which is similar to the circulation from the two-dimensional PIV results, 6.87 (see Gan & Nickels, 2010).

[7] If one produces a large number of turbulent vortex rings from a circular orifice, and does an ensemble average, the resultant velocity field is approximately axisymmetric.

[8] Recall that the raw data is stored in the Cartesian coordinates; towards smaller radii, there are less data points.

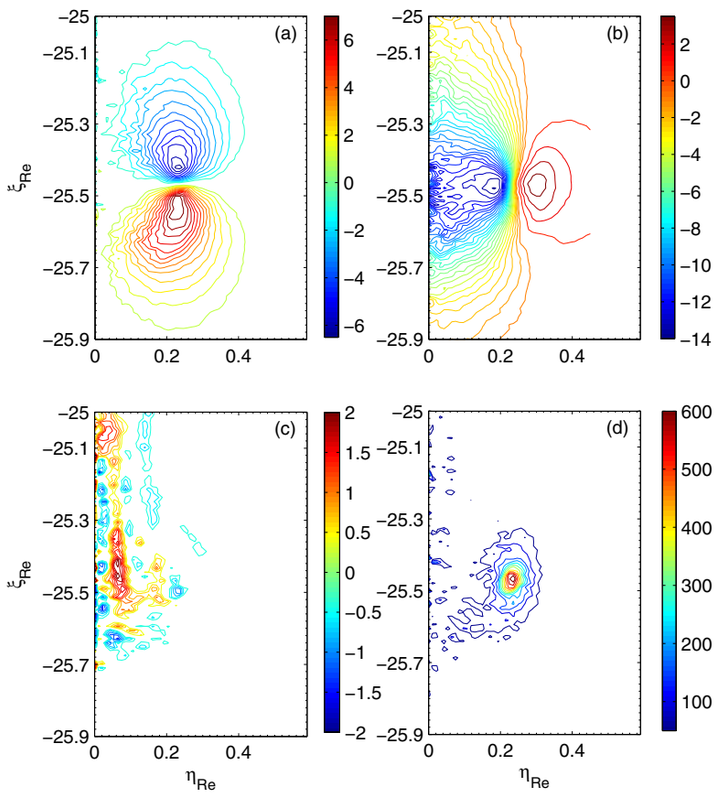

Fig. 20. The mean structures of velocity and vorticity calculated by the azimuthally averaging process: averaging along the θ direction in similarity coordinates. Contours shown are U_θ (radial), V_θ (axial), W_θ (azimuthal) and $\widehat{\omega}_\theta$ (azimuthal) in (a), (b), (c) and (d), respectively; the subscript θ denotes that the corresponding quantity is calculated by the azimuthally averaging process.

If the azimuthally averaged velocity components make sense it is also possible to compare the turbulence quantities, one can refer to Gan et al. (2011) for more details.

The turbulence production is believed to be closely related to the vortex stretching, this mechanism is expected to take place in the ring core and bubble windward regions (Gan & Nickels, 2010). The stretching effect can be assessed via the vorticity equation. In Cartesian coordinates, the stretching term $(\vec{\omega} \cdot \nabla)\,\vec{u}$ represents the vortex stretching in three principal directions, S_i, S_j, S_k:

$$\begin{pmatrix} S_i \\ S_j \\ S_k \end{pmatrix} = (\vec{\omega} \cdot \nabla) \begin{pmatrix} u_i \\ u_j \\ u_k \end{pmatrix}, \tag{17}$$

on ω_i, ω_j, ω_k respectively.

Because the flow field of a vortex ring is close to axisymmetric, the stretching of the vortex tubes in the windward bubble surface is expected to be orientated in the radial direction (due to the mean velocity direction). To better illustrate the stretching effect, the vorticity and the stretching vector in equation 17 are transferred from Cartesian coordinates to cylindrical coordinates, as for velocities: $\omega\,(i,j) \mapsto \omega\,(\theta,r)$, $S\,(i,j) \mapsto S\,(\theta,r)$, ω_k and S_k are unaffected.

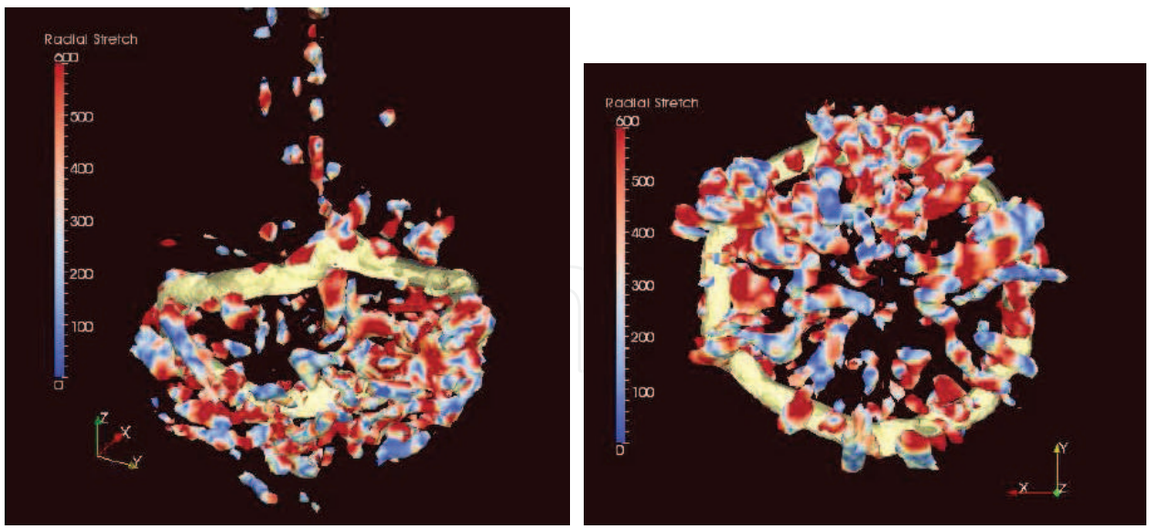

Fig. 21. Vortex ring core $\omega_\theta = -140s^{-1}$ shown by the yellow coloured isosurface; and the radial vorticity $\omega_r = \pm 30s^{-1}$. The colour code on the ω_r isosurface shows the magnitudes of the radial stretching term $|S_r|$, with the positive valued S_r dyed on the positive ω_r and negative valued S_r dyed on the negative ω_r.

The radial vorticity ω_r is plotted in figure 21, with the radial direction stretching term S_r coloured on the isosurface. Figure 21 supports the expectation that vortices are being stretched in the radial direction and this stretching mechanism prevails on the windward side of the bubble. The compression of vorticity, i.e. the correlation of the opposite sensed vorticity and the stretching value, is much weaker (less than 20%) compared with stretching and is not shown here. The vorticity in the windward bubble region can also be seen in figure 17, in Cartesian coordinates. The streamwise stretching, which has been mentioned in section 2.4, is believed to be responsible for the turbulence production in the wake region however this is very small overall.

3. Conclusions

The first part of this chapter introduces the 2D3C working principle of stereoscopic PIV and its calibration procedure and its self-calibration to increase the accuracy level. The second part of the chapter presents an application of stereoscopic PIV for reconstructing a fully three-dimensional vortex ring. It has shown that by fixing the laser sheet position and hence the two cameras' FOV, and reconstructing the fully three-dimensional velocity field by Taylor's hypothesis, the accuracy of the results is limited. In other words, due to the intrinsic nature of Taylor's hypothesis, the resultant velocity field is never really instantaneous. However, there are various aspects which can increase the potential accuracy of such reconstruction and thus deserve further discussion.

3.1 Possible accuracy improvements

In order to freeze the ring structure better, the results of equation 11 needs to be closer to zero. Nevertheless, it is expected that for fully turbulent vortex ring, the level of turbulence intensity u' scales with Reynolds number (because $u' \sim U_p$), hence scales with vortex ring circulation

Γ and the advection speed u_t. Simply increasing Reynolds number will not improve the situation. Certain treatments independent of the ring will be necessary. A possible way is to move the PIV measurement (cameras and the laser sheet together) against the ring advection direction - an 'active scanning' process. Equation 11 shows that by simply moving the PIV measurement plane at the same speed as the ring, it can bring down the ratio u'/u_t significantly (doubling the denominator). Moreover, to resolve the wake correctly, an active scanning seems to be compulsory.

The next question is that how fast the scan speed is optimal. Definitely scan with an infinite speed gives no error. However, first it is not allowed, even it is capable to; second, it may not be necessary in applications where Reynolds number is not too high. A proper quantity can be searched to judge what scan speed gives satisfactory accuracy level. For instance, a possible candidate can be the spatial velocity correlation tensor, or the structure function, which is expected to converge as the scan speed increases. Thus, a scan speed can be considered adequate and economic (in terms of hardware requirement and computational expense), above which the increase of the accuracy is less significant while the cost-benefit ratio is high. In different flow problems, the optimal scan speed is expected to vary. Similar to the accuracy assessment given in section 2.3, a crude estimation of the scan speed could be made from the eddy turn over time: if the mean flow is of the only interest, a moderate scan speed should be enough; if small eddies are to be resolved, higher speed is required.

It has been pointed out that there exists an upper limit of the active scanning speed, it is not allowed to go to infinity. In other words, it is never possible to capture a truly frozen flow field. It is because if the flow is really frozen, there will be no particle displacement, thus the PIV fails to work. In order to allow a particle displacement to compute the velocity, a minimum time duration of PIV Δt has to be given at one measurement station along the scanning path. In this aspect, this PIV Δt, despite its shortness - in order of millisecond, limits the highest scan speed.

Nevertheless there is a potential solution for this limitation: a second stereoscopic PIV system can be introduced, aligning with the first system in the scanning path, and with a spacing l to the first one; see figure 22.[9] Thus the value of l/U_{scan} effectively gives the PIV Δt. Theoretically, this dual-system arrangement allows the choice of the U_{scan} value to a much higher value: at a fixed U_{scan}, PIV Δt can be adjusted by setting the spacing l between the two systems (two laser sheets) very carefully. The highest scan speed in this case is then limited by the required spatial resolution in the scan direction, which is much more relaxed than the limit from the particle displacements. The high speed cameras available nowadays can work at several *kHz* frame rates, which allows very high scan speed while maintaining good spatial resolution in the scanning direction. By choosing a very high value of U_{scan}, one approaches a truly frozen and instantaneous flow structure.

3.2 Comparison to tomographic PIV

The state-of-the-art tomographic PIV is also a candidate to provide truly instantaneous three-dimensional velocity information of a flow field. Its working principle is developed

[9] Vortex ring study is definitely not the only customer of this method. It can be applied to many general flow problems. Figure 22 shows an application on a turbulent jet flow.

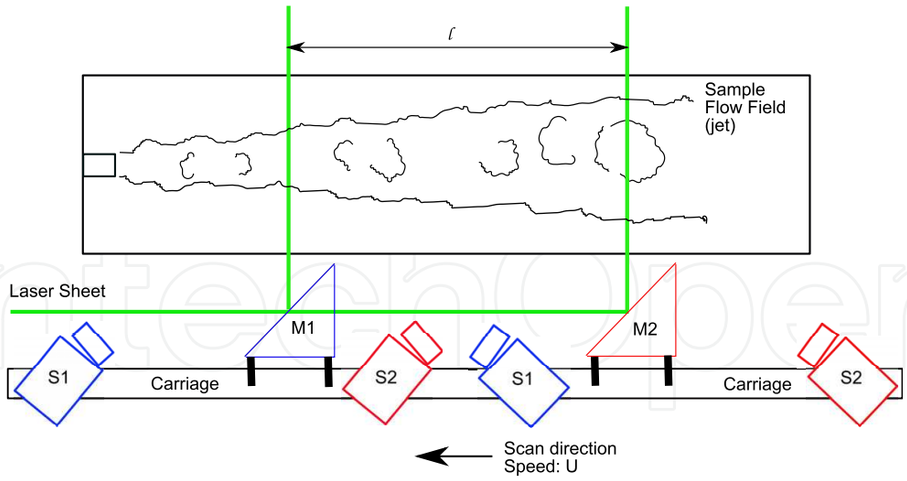

Fig. 22. A simple sketch of the proposed scan system including dual stereo recording PIV systems, denoted in the figure by S1 (M1) and S2 (M2). The two systems can be mounted on a rail-carriage system, so that they can move together, at a designed speed U_{scan}. M1 can be a beam splitter. l denotes the spacing of the two systems, U denotes the scan speed U_{scan}. This scan system can be applied to any flow problem. A sample flow field - turbulent jet flow - is shown.

from the medical tomographic applications. The illuminated particle volume is viewed by several cameras (the more cameras used, the more accurate the results will be) at the same time. Then the *most-likely* three-dimensional particle distribution in the volume is reconstructed by the tomographic algorithm, based on the intersections of lines of sight giving the estimated particle location; see Elsinga et al. (2006) for more details. Albeit its robustness of measuring the truly instantaneous three-dimensional velocity field, its major weakness lies in its relatively low signal-noise ratio compared to the two-dimensional and stereoscopic PIV. It is because tomographic reconstruction is an inverse problem, i.e. the three-dimensional information is reconstructed from its two-dimensional projections, regardless of how many cameras are used, the error or the noise (in particular ghost particles, which will be discussed later below) is inevitable.

In addition to this intrinsic problem, tomographic PIV would also encounter some difficulties when a large volume of flow is to be examined. To reach the same FOV as the current experiment, a minimum required FOV will be $100mm^3$. This means that first of all, this volume needs to be illuminated; the emission intensity of practical lasers would be very weak when it is diffused to such a large volume.

Second, it would be extremely difficult for the cameras to be focused on such a deep FOV (which means the aperture needs to be very small) while accepting enough light during very short laser emission time. Therefore, if tomographic PIV is to be used, one can only produce small scaled flows, but small scaled flow reduces the spatial resolution, probably to an undesired level. The spatial resolution is also limited by the interrogation volume (similar to interrogation window for planner PIV configuration) size. For the practical sparsity level of particle field, the commonly acceptable interrogation volume size is typically 48 $voxel^3$, while the planner PIV can easily reach 16 $pixel^2$. Thus the absolute spatial resolution

limit of tomographic PIV is normally much lower than that of stereoscopic PIV with typical $voxel - pixel$ ratio of unit.

Moreover, although tomographic PIV can also provide temporal-resolved information, its working principle requires iteration and can only give *the most likely* (not true) particle distribution in the FOV (due to the intersection of lines of sight giving ghost particles, although the cross-correlation signals of which are weaker). This is a considerable error source of tomographic PIV, among others. In addition, compared with the active scanning method, with the same amount of information[10], to resolve temporal information, it must either be more computational expensive or less accurate.

4. References

Archer, P. J., Thomas, T. G. & Coleman, G. N. (2008). Direct numerical simulation of vortex ring evolution from the laminar to the early turbulent regime., *J. Fluid Mech.* 598: 201–226.

Bergdorf, M., Koumoutsakos, P. & Leonard, A. (2007). Direct numerical simulations of vortex rings at Re_Γ =7500., *J. Fluid Mech.* 581: 495–505.

Elsinga, G. E., Scarano, F., Wieneke, B. & van Oudheusden, B. W. (2006). Tomographic particle image velocimetry., *Exp. Fluids* 41: 933–947.

Gan, L. (2010). *PhD Dissertation: An experimental study of turbulent vortex rings using particle image velocimetry*, University of Cambridge.

Gan, L. & Nickels, T. B. (2010). An experimental study of turbulent vortex rings during their early development, *J. Fluid Mech.* 649: 467–496.

Gan, L., Nickels, T. B. & Dawson, J. R. (2011). An experimental study of turbulent vortex rings during: a three-dimensional representation, *Exp. Fluids* 51: 1493–1507.

Glezer, A. (1988). On the formation of vortex rings., *Phys. Fluids* 31: 3532–3542.

Glezer, A. & Coles, D. (1990). An experimental study of turbulent vortex ring., *J. Fluid Mech.* 211: 243–283.

Lavision (2007). *Product Manual-Davis 7.2 Software.*, Lavision GmbH, Gottingen.

Maxworthy, T. (1977). Some experimental studies of vortex rings., *J. Fluid Mech.* 81: 465–495.

Prasad, A. K. (2000). Stereoscopic particle image velocimetry., *Exp. Fluids* 29: 103–116.

Raffel, M., Willert, C., Wereley, S. & Kompenhans, J. (2007). *Particle Image Velocimetry-A Practical Guide, Second Edition*, Springer-Verlag, Berlin.

Saffman, P. G. (1978). The number of waves on unstable vortex rings., *J. Fluid Mech.* 84: 625–639.

Shariff, K., Verzicco, R. & Orlandi, P. (1994). A numerical study of three-dimensional vortex ring instabilities: viscous corrections and early nonlinear stage., *J. Fluid Mech.* 279: 351–375.

Taylor, G. I. (1938). The spectrum of turbulence., *Proc. R. Soc. London, Ser. A* 164: 476–490.

Townsend, A. A. (1976). *The structure of turbulent shear flow. Second Edition.*, Cambridge University Press, Cambridge.

Widnall, S. E. & Tsai, C. Y. (1977). The instability of the thin vortex ring of constant vorticity., *Philo Trans R Soc Lond A* 287: 273–305.

[10] If two scan systems are used, four cameras are needed, which is the same as tomo-PIV; while only two cameras are needed for one system scanning, which is only half of the information amount.

Wieneke, B. (2005). Stereo-piv using self-calibration on particle images., *Exp. Fluids* 39: 267–280.

Wieneke, B. (2008). Volume self-calibration for 3d particle image velocimetry., *Exp. Fluids* 45: 549–556.

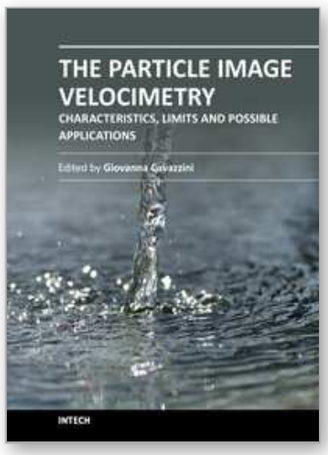

The Particle Image Velocimetry - Characteristics, Limits and Possible Applications

Edited by PhD. Giovanna Cavazzini

ISBN 978-953-51-0625-8
Hard cover, 386 pages
Publisher InTech
Published online 23, May, 2012
Published in print edition May, 2012

The Particle Image Velocimetry is undoubtedly one of the most important technique in Fluid-dynamics since it allows to obtain a direct and instantaneous visualization of the flow field in a non-intrusive way. This innovative technique spreads in a wide number of research fields, from aerodynamics to medicine, from biology to turbulence researches, from aerodynamics to combustion processes. The book is aimed at presenting the PIV technique and its wide range of possible applications so as to provide a reference for researchers who intended to exploit this innovative technique in their research fields. Several aspects and possible problems in the analysis of large- and micro-scale turbulent phenomena, two-phase flows and polymer melts, combustion processes and turbo-machinery flow fields, internal waves and river/ocean flows were considered.

How to reference

In order to correctly reference this scholarly work, feel free to copy and paste the following:

L. Gan (2012). Stereoscopic PIV and Its Applications on Reconstruction Three-Dimensional Flow Field, The Particle Image Velocimetry - Characteristics, Limits and Possible Applications, PhD. Giovanna Cavazzini (Ed.), ISBN: 978-953-51-0625-8, InTech, Available from: http://www.intechopen.com/books/the-particle-image-velocimetry-characteristics-limits-and-possible-applications/stereoscopic-piv-and-its-applications-on-reconstruction-3d-flow-field

INTECH
open science | open minds

InTech Europe
University Campus STeP Ri
Slavka Krautzeka 83/A
51000 Rijeka, Croatia
Phone: +385 (51) 770 447
Fax: +385 (51) 686 166
www.intechopen.com

InTech China
Unit 405, Office Block, Hotel Equatorial Shanghai
No.65, Yan An Road (West), Shanghai, 200040, China
中国上海市延安西路65号上海国际贵都大饭店办公楼405单元
Phone: +86-21-62489820
Fax: +86-21-62489821

IntechOpen